American Mineralogist, Volume 104, pages 897–904, 2019

High-pressure phase transitions of clinoenstatite

John D. Lazarz[1,*], Przemyslaw Dera[2], Yi Hu[2,3], Yue Meng[4], Craig R. Bina[1], and Steven D. Jacobsen[1]

[1]Department of Earth and Planetary Sciences, Northwestern University, Evanston, Illinois 60208, U.S.A.
[2]Hawaii Institute of Geophysics and Planetology, School of Ocean and Earth Science and Technology, University of Hawai'i at Manoa, Honolulu, Hawaii 96822, U.S.A.
[3]Department of Geology and Geophysics, School of Ocean and Earth Science and Technology, University of Hawai'i at Manoa, Honolulu, Hawaii 96822, U.S.A.
[4]HPCAT, Advanced Photon Source, Argonne National Laboratory, Argonne, Illinois 60439, U.S.A.

Abstract

Clinoenstatite ($Mg_2Si_2O_6$) undergoes a well-known phase transition from a low-pressure form (LPCEN, space group $P2_1/c$) to a high-pressure form (HPCEN, space group $C2/c$) at ~6 GPa. High-pressure structure refinements of HPCEN were carried out based on single-crystal X-ray diffraction experiments between 9.5 and 35.5 GPa to determine its *P-V* equation of state and structural evolution over an expanded pressure range relevant to pyroxene metastability. The best-fit isothermal equation of state to our data combined with the five data points between 5.34 and 7.93 GPa from Angel and Hugh-Jones (1994) yields a second-order Birch-Murnaghan equation with K_{T0} = 121(2) GPa and V_0 = 403.9(5) Å^3 (with K'_{T0} = 4 implied). Further reduction of misfit upon fitting a third-order Birch-Murnaghan equation is not significant at the 90% confidence level. At ~45 GPa, a transition from HPCEN to a $P2_1/c$-structured polymorph (HPCEN2) was observed, which is isostructural to the $P2_1/c$ phase recently observed in diopside ($CaMgSi_2O_6$) at 50 GPa (Plonka et al. 2012) and in clinoferrosilite ($Fe_2Si_2O_6$) at 30–36 GPa (Pakhomova et al. 2017). Observation of HPCEN2 in $Mg_2Si_2O_6$ completes the third apex of the pyroxene quadrilateral wherein HPCEN2 is found, facilitating a broader view of clinopyroxene crystal chemistry at conditions relevant to metastability in the Earth's mantle along cold subduction geotherms.

Keywords: $MgSiO_3$, clinoenstatite, enstatite, pyroxene, single-crystal X-ray diffraction

Introduction

Pyroxenes are a major component of the Earth's crust and upper mantle, constituting around 25% by volume of the pyrolite model from 100–400 km depth (Ringwood 1976; Akaogi and Akimoto 1977). The components of both orthopyroxene $(Mg,Fe)SiO_3$ and clinopyroxene-$CaMgSi_2O_6$ are incorporated into pyrope and majoritic garnet at depths from 300–500 km, however under the colder conditions along subducting slabs it is possible for metastable pyroxenes to persist deep in the upper mantle (e.g., Hogrefe et al. 1994; Bina 2013; Nishi et al. 2013; Van Mierlo et al. 2013; Agrusta et al. 2014; Finkelstein et al. 2015; King et al. 2015). Pyroxenes penetrating the mantle to such depths could potentially undergo further phase transitions impacting subducting slab mineralogy and mantle dynamics.

The major pyroxenes relevant to mafic-ultramafic rocks and the Earth's upper mantle are characterized by single chains of corner-sharing SiO_4 tetrahedra interconnected by MO_6 octahedra containing M cations Mg, Fe, or Ca forming the pyroxene compositional quadrilateral with end-members enstatite (En, $Mg_2Si_2O_6$), ferrosilite (Fs, $Fe_2Si_2O_6$), diopside (Di, $MgCaSi_2O_6$), and hedenbergite (Hd, $CaFeSi_2O_6$) (Morimoto et al. 1989). Pyroxenes along the En-Fs join are orthorhombic (*Pbca*), and hence known as orthopyroxenes, whereas Ca-bearing pyroxenes in the quadrilateral are monoclinic and hence called clinopyroxenes (Cpx). Ca-rich Cpx crystallizes in $C2/c$ (augite) while Ca-poor Cpx crystallizes in $P2_1/c$ (pigeonite).

Orthoenstatite-$Mg_2Si_2O_6$ (OEN) is a major phase of peridotite and was found to transform to a monoclinic, high-pressure clinoenstatite (HPCEN) with space group $C2/c$ along a phase boundary corresponding to ~200–250 km depth (e.g., Pacalo and Gasparik 1990; Angel et al. 1992), suggesting that the transformation might be associated with upper-mantle seismic discontinuities, namely the Lehman discontinuity or the X-discontinuity (e.g., Revenaugh and Jordan 1991; Angel et al. 1992; Deuss and Woodhouse 2004; Kung et al. 2004; Ferot et al. 2012). In experiments, the HPCEN phase quenches to the monoclinic, low-pressure clinoenstatite (LPCEN) with space group $P2_1/c$, which is however rare in nature (e.g., Poldervaart and Hess 1951; Shiraki et al. 1980).

On compression, the transformation from LPCEN to HPCEN at 300 K varies from 6 to 8 GPa, depending on Fe-content, water content, and stress (e.g., Ross and Reynard 1999; Jacobsen et al. 2010). With both OEN and LPCEN transforming to HPCEN at pressures below 10 GPa, it has been presumed that HPCEN is the stable phase of $(Mg,Fe)_2Si_2O_6$ below ~250 km depth. The reference physical properties of HPCEN are not well constrained because it is not a quenchable phase, however, in situ sound velocity measurements by Kung et al. (2004) were used to determine its adiabatic elastic moduli at a reference pressure of 6.5 GPa, with K_{S0} = 156.7(8) GPa and G_0 = 98.5(4) GPa. Previous volume-compression studies

* Present address: Shock and Detonation Physics, Los Alamos National Laboratory, Los Alamos, NM 87545, U.S.A. E-mail: lazarz@lanl.gov

0003-004X/19/0006–897$05.00/DOI: https://doi.org/10.2138/am-2019-6740

across the LPCEN-HPCEN transition estimated the zero-pressure isothermal bulk modulus of HPCEN to be $K_{T0} \approx 118$ GPa (Jacobsen et al. 2010) and $K_{T0} = 104(6)$ GPa (Angel and Hugh-Jones 1994), but these studies relied on extrapolation from very few data points over a very limited pressure range of 6–8 GPa.

We investigated the volume and structural compression behavior of HPCEN from single-crystal X-ray diffraction measurements at 10–35 GPa. At 45 GPa, we observed a new phase of $Mg_2Si_2O_6$ with space group $P2_1/c$. This phase, a second monoclinic high-pressure clinoenstatite (HPCEN2) is isostructural to the high-pressure clinopyroxene found in clinoferrosilite-$Fe_2Si_2O_6$ at 30–36 GPa (Pakhomova et al. 2017) and in diopside-$CaMgSi_2O_6$ at ~50 GPa (Plonka et al. 2012; Hu et al. 2017), providing further evidence that the HPCEN2 structure is common to phases in the pyroxene quadrilateral. The pressure-temperature-compositional dependence of the HPCEN to HPCEN2 transition has implications for understanding potential pyroxene metastability along cold subduction geotherms and may impact models of slab dynamics.

Experimental methods

High-pressure X-ray diffraction

Synthesis of LPCEN single crystals used in this study was described previously (Jacobsen et al. 2010). Briefly, powdered MgO and SiO_2 starting materials were mixed in 1:1 molar proportion and heated at 950 °C for 6 h in a flux of V_2O_5, MoO_3, and Li_2CO_3 in molar proportions of 1:7:9. The run products consisted primarily of low-clinoenstatite, with minor amounts of orthoenstatite and quartz. LPCEN crystals were selected for diffraction experiments using Raman spectroscopy to confirm the presence of the 369 and 431 cm^{-1} vibrational bands, the distinguishing feature from orthoenstatite (Ulmer and Stalder 2001).

High-pressure, single-crystal X-ray diffraction (XRD) experiments were carried out at HPCAT, Sector 16 experimental station 16ID-B of the Advanced Photon Source (APS), Argonne National Laboratory (ANL). Diamond-anvil cell XRD measurements spanned the pressure range 9.5 to 50 GPa. A rhenium gasket with an initial thickness of 250 μm was pre-indented to ~40 μm using 300 μm culet Bohler-Almax type diamond anvils. Two 30 μm diameter, approximately 20 μm thick, single crystals were loaded into the sample chamber along with two ruby spheres. Differential stresses within the sample chamber were minimized by loading neon as a pressure medium using the GSECARS/COMPRES gas loading system (Rivers et al. 2008). The pressure was determined using the ruby fluorescence method (Mao et al. 1986).

The diffraction experiments used a monochromatic X-ray beam with wavelength 0.351453 Å, focused with a Kirkpatrick-Baez mirror system to ~0.005 mm, full-width half maximum, in both horizontal and vertical directions. A MAR165 charge-coupled device (CCD) detector was placed roughly 170 mm away from the sample, and LaB_6 powder was used to calibrate the distance and tilt of the detector. The diffraction-accessible angular opening of the diamond cell was ±33° during the data collection. On increasing pressure, a series of step and wide-step ω-scans were collected. Step scans involved 1° angular increments, while wide-step scans had 16.5° angular increments. The exposure time was at 1 s per degree. After collection of step and wide-step ω-exposures at the zero detector position, more wide-step ω-exposures were recorded with the detector translated horizontally, perpendicular to the X-ray beam by 70 mm. Exposure rates for the off-center detector positions were 2 s per degree. Step scans were used to obtain intensities for structural refinement.

Diffraction images were analyzed using GSE_ADA and RSV software packages (Dera 2013). Least-squares structure refinements were performed at every pressure point using SHELXL (Sheldrick 2008). In all refinements, displacement parameters were treated as isotropic and site occupancy factors were fixed with the tetrahedral sites fully occupied by Si and the two octahedral sites occupied by Mg. Neutral scattering factors were used. Refinements statistics are listed in Table 1. Structure refinement results can be found in Supplementary[1] CIF files.

Density functional theory calculations

To obtain some thermodynamic interpretation of the three phases observed in the experiments, we performed a series of crystal structure optimizations and electronic structure calculations using density functional theory (DFT), as implemented in the Vienna Ab Initio Simulation Package (VASP) version 5.4 (Kresse and Hafner 1993), controlled by MedeA interface, ver. 2.22.1. All density functional calculations used the Perdew-Burke-Ernzerhof (PBE) generalized gradient approximation (GGA) (Perdew et al. 1996). The projector augmented wave (PAW) method (Blöchl 1994) was used to treat the core states with a plane wave basis set. The Si $3s^2/3p^2$, O $2s^2/2p^4$, and Mg $3s^2$ electrons were treated explicitly using the PAW-PBE Si, O, and Mg POTCARs, which are available in MedeA. The energy cutoff was set to be 520 eV. The **k**-point grids were generated using the Γ-centered scheme, with 2 **k**-points per angstrom, leading to 2 × 2 × 3 mesh. Temperature effects were not included in the DFT calculations. Similar DFT-based approach has been demonstrated to reasonably well reproduce the phase transition boundaries in the $MgSiO_3$ pyroxene system in earlier studies (Yu and Wentzcovitch 2009).

Results and discussion

Single-crystal X-ray diffraction experiments performed between 9.5 and 50 GPa revealed two clinoenstatite phases. The first phase, observed at six pressure points spanning 9.5–35.5 GPa, was successfully indexed using the monoclinic $C2/c$ space group. Crystal reflections remained sharp, in this pressure range, suggesting a lack of deviatoric stresses. Variation of the unit-cell parameters with pressure (Table 2) shows a continuously decreasing trend up to 35.5 GPa. Refined lattice parameters agree well with the previously reported high-pressure clinoenstatite $C2/c$ phase (Angel and Hugh-Jones 1994; Shinmei et al. 1999). At 45 GPa, clinoenstatite underwent a sudden volume decrease indicating that a first-order phase change occurred between 41.34 and 45 GPa. Quality of data collected around this pressure range is too low for quantitative analysis. The next viable data point was collected at 50.2 GPa. Data quality from this single pressure point is too low for single-crystal structure refinement, however, the measured lattice parameters and accompanying DFT calculations indicate the transition from HPCEN to HPCEN2 as in diopside (Plonka et al. 2012; Hu et al. 2016) and clinoferrosilite (Pakhomova et al. 2017). Structural evolution of clinoenstatite with pressure is shown in Figure 1.

The lattice parameters and volume of HPCEN as a function of pressure (Table 2) were fitted with Birch-Murnaghan

Table 1. Structural refinement statistics for HPCEN

P (GPa)	9.5(1)	10.4(1)	17.0(2)	24.4(2)	30.1(3)	35.5(7)
Measured reflections	768	497	346	406	401	384
Unique reflections	442	218	153	159	160	155
$F_o>4\sigma(F_o)$	441	218	151	159	121	153
R_{int}	7.90%	9.19%	14.97%	8.55%	8.975	7.90%
Rw for $F_o>4\sigma(F_o)$	5.22%	5.89%	8.11%	7.01%	7.04%	6.01%
R_{all}	5.22%	5.89%	8.11%	7.01%	8.40%	6.09%
$wR2$	15.34%	15.71%	21.45%	16.44%	19.60%	16.52%
GooF	1.168	1.223	1.103	1.168	1.102	1.237
No. parameters	21	21	21	21	21	21
Space group	$C2/c$	$C2/c$	$C2/c$	$C2/c$	$C2/c$	$C2/c$
Z	4	4	4	4	4	4
Absorption coefficient	0.152	0.079	0.159	0.164	0.169	0.172

Table 2. Lattice parameters of high-pressure clinoenstatite ($Mg_2Si_2O_6$, HPCEN-$C2/c$) and HPCEN2-$P2_1/c$ at various pressures

P (GPa)	Space group	a (Å)	b (Å)	c (Å)	β (°)	V (Å^3)
9.5(1)	$C2/c$	9.163(2)	8.587(1)	4.875(1)	101.325(1)	376.2(2)
10.4(1)	$C2/c$	9.144(2)	8.5452(9)	4.8807(9)	101.25(2)	374.1(2)
17.0(2)	$C2/c$	8.965(3)	8.443(1)	4.847(1)	100.91(3)	360.3(2)
24.4(2)	$C2/c$	8.871(2)	8.3397(9)	4.7940(9)	100.46(2)	348.8(2)
30.1(3)	$C2/c$	8.804(2)	8.244(1)	4.749(1)	100.31(2)	339.2(2)
35.5(7)	$C2/c$	8.739(3)	8.190(1)	4.714(1)	100.22(2)	332.1(2)
50.2(9)	$P2_1/c$	8.688(2)	7.828(2)	4.5840(9)	100.46(2)	306.6(1)

equations of state. The HPCEN-*C*2/*c* reference volume (V_0) was refined during the least-squares fitting procedure because HPCEN-*C*2/*c* is unquenchable (Angel et al. 1992; Ross and Reynard 1999). Fitting was performed using the Burnman Python library (Cottaar et al. 2014) as well as using our own code. The best-fit isothermal equation of state to our data alone yields a second-order Birch-Murnaghan equation (BM2, for which K'_{T0} is identically equal to 4) with K_{T0} = 129(2) GPa and V_0 = 401.2(6) Å^3.

In an attempt to fill in the gap in our data set below pressures of 9.5 GPa, we combined our data with the lower-pressure data at 5.34–7.93 GPa from Angel and Hugh-Jones (1994), yielding a second-order Birch-Murnaghan equation (for which K'_{T0} is identically equal to 4) with K_{T0} = 121(2) GPa and V_0 = 403.9(5) Å^3. A third-order Birch-Murnaghan equation of state (BM3) fitted to the merged data set gives the parameters: V_0 = 406(1) Å^3, K_{T0} = 103(8) GPa, and K'_{T0} = 5.4(6). However, further reduction of misfit upon fitting a third-order Birch-Murnaghan equation is not significant at the 90% confidence level, as determined from an F-test (Bevington and Robinson 2003). The second-order fit to the combined data set is thus our preferred equation of state for HPCEN. Both BM2 and BM3 fits to the HPCEN compression data are shown in Figure 2.

For comparison, we also performed EoS fitting following the procedure outlined in Jacobsen et al. (2010) wherein the lowest pressure data point is treated as the reference pressure by assigning it a value of 0 GPa (with associated error in volume and pressure from the measurement) and adding each pressure step to subsequent points. Since the minimum pressure point in our data set combined with Angel and Hugh-Jones (1994) is 5.34 GPa, the fitted values of V and K_T are obtained at 5.34 GPa as the reference pressure. Following this procedure and using the BM2 yields $V_{5.34}$ = 387.8(2) Å^3 and $K_{5.34}$ = 140(2) GPa. Using these values as V_0 and K_{T0} (with K'_{T0} = 4 implied) at P = –5.34 GPa yields calculated zero-pressure parameters $V_{0\,calc}$ = 404.1 Å^3 and $K_{0\,calc}$ = 119 GPa, which are within uncertainty of our best-fit result in the second-order fit to reference P = 0, which gave V_0 = 403.9(5) Å^3 and K_{T0} = 121(2) GPa.

In Figure 3, we show *P*-*V* data as normalized stress, $F_E = P/3f_E(1 + 2f_E)^{5/2}$ vs. Eulerian finite strain, $f_E = [(V_0/V)^{2/3} - 1]/2$ for the BM3 with V_0 = 406(1) Å^3. The positive slope and linear fit of the F_E-f_E plot illustrate the large V_0 = 406(1) Å^3 resulting from the BM3 fit results in a $K'_0 > 4$, although we note the improvement in fit over BM2 is statistically insignificant.

The equation of state parameters for HPCEN-*C*2/*c* are summarized in Table 3, with covariance plotted in Figure 4. Reported values from other studies fall largely within the estimated standard deviations of our results. The large K'_0 = 6.6 (fixed) in Angel and Hugh-Jones (1994) was adopted from the value fitted to their LPCEN equation of state and is inconsistent with our BM3 fit to the combined data sets for HPCEN (Fig. 4).

The variation in linear dimension, l, of a material can be expressed as linear compressibility, defined as $\beta_l = (-l)^{-1}(\delta l/\delta P)$. For linear parameters such as a, b, c we assess their compressibility by treating the cube of each parameter as volume in a Birch-Murnaghan EoS fitting procedure (Angel et al. 2014). The choice of EoS order was again made based on the F_E-f_E plot. A horizontal linear fit to the F_E-f_E plot for all unit-cell parameters prompted our selection of a second-order Birch-Murnaghan equation of state, K'_0 = 4. For HPCEN-*C*2/*c*, our fitted linear moduli to a, b, c, and $a\sin\beta$ are 99(3), 101(2), 158(7), and 115(4) GPa, respectively. Subsequent axial com-

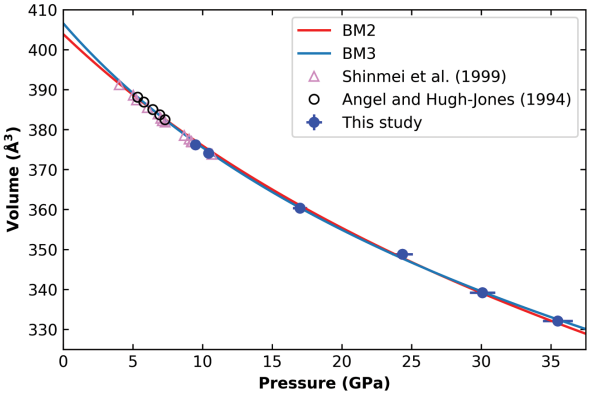

FIGURE 2. Comparison of variation in unit-cell volume as a function of pressure in anhydrous $MgSiO_3$ high-pressure clinoenstatite (HPCEN). A second-order (red curve) and third-order (blue curve) Birch-Murnaghan equation of state fitted to the data from this study combined with Angel and Hugh-Jones (1994). (Color online.)

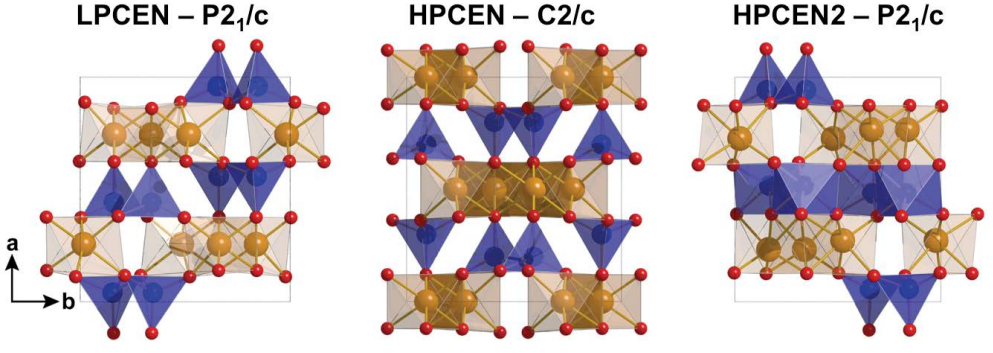

FIGURE 1. The three monoclinic structures of $Mg_2Si_2O_6$ (clinoenstatite). (**left**) Low-pressure clinoenstatite (LPCEN) stable up to ~6 GPa. (**middle**) The unquenchable high-pressure clinoenstatite (HPCEN) stable at 6–45 GPa. (**right**) High-pressure clinoenstatite-2 (HPCEN2), observed at ~45 GPa in the current study. HPCEN2 structure shown here has been calculated using DFT. The edge-sharing Mg octrahedra are shown in yellow and corner-sharing silica tetrahedra are shown in blue. The HPCEN2 phase features edge-sharing octahedral Si, also shaded blue. (Color online.)

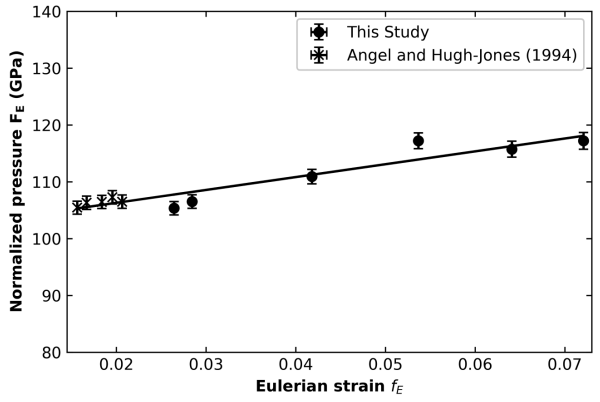

FIGURE 3. Normalized stress F_E vs. the Eulerian strain f_E for HPCEN shown for the third-order Birch-Murnaghan fit.

TABLE 3. Equation of state parameters for high-pressure clinoenstatite (HPCEN)

P-range (GPa)	V_0 (Å^3)	K_{T0} (GPa)	K'_{T0} (GPa)	ρ_0 (g/cm^3)	Reference
9.5–35.5	401.2(6)	129(2)	4 (implied)	3.324(5)	This study
5.3–35.5	403.9(5)	121(2)	4 (implied)	3.302(4)	This study[a]
5.3–35.5	406(1)	103(8)	5.4(6)	3.285(8)	This study[a]
7.1–8.06	404	118	6.1	3.302	Jacobsen et al. (2010)
4.0–10.7	405(2)	106(17)	5(3)	3.292(14)	Shinmei et al. (1999)
5.3–8.0	406(1)	104(6)	6.6 (fixed)	3.288(9)	Angel and Hugh-Jones (1994)

[a] This study combined with the data from Angel and Hugh-Jones (1994).

pressibility values are $\beta_a = 10.1(3) \times 10^{-3}$, $\beta_b = 9.9(2) \times 10^{-3}$, $\beta_c = 6.3(3) \times 10^{-3}$, $\beta_{asin\beta} = 8.7(3) \times 10^{-3}$ GPa^{-1}.

Volume and axial compression of our HPCEN-*C*2/*c*, as compared to pyroxene phases belonging to the hedenbergite-diopside-ferrosilite-enstatite, $CaFeSi_2O_6$-$MgCaSi_2O_6$-$Fe_2Si_2O_6$-$Mg_2Si_2O_6$, quadrilateral system (Morimoto et al. 1989) are plotted in Figure 5. The evolution of HPCEN-*C*2/*c* lattice parameters with pressure differs slightly from that of other familial pyroxenes. Clinopyroxenes tend to follow the characteristic axial compressibility scheme $\beta_b > \beta_c \approx \beta_a > \beta_{asin\beta}$ (Angel and Hugh-Jones 1994; Tribaudino et al. 2001; Nestola et al. 2004; Hu et al. 2015; Pakhomova et al. 2017) however, our results show HPCEN-*C*2/*c* follows the axial compressibility scheme $\beta_a \approx \beta_b > \beta_{asin\beta} \geq \beta_c$.

With an exception for a minor deflection in the stiffness of *a* beginning around 12 GPa, each axial direction maintains a steady compression trend relative to the other parameters. In our observed compression scheme, the decrease in volume between 9.5 and 35.5 GPa is due primarily to compression of the *a* and *b* axes, while the stiffer *a*sinβ and *c* parameters contract relatively little. The different anisotropy scheme of the HPCEN-*C*2/*c* phase with respect to other pyroxenes shows that the HPCEN-*C*2/*c* structure evolves differently with pressure than other pyroxenes.

Within the quadrilateral family, the *b* dimension is unique with the magnitudes remaining relatively clustered and showing similar compressibilities throughout the observed pressure range. This observation breaks down for the other lattice parameters *a*, *c*, and β. Other quadrilateral pyroxenes differ from HPCEN-*C*2/*c* where lattice parameter *a* is significantly shorter than other pyroxenes. Lattice parameters, among pyroxenes in the quadrilateral family, are also dispersed in magnitude for *c* and β. Compression behavior of HPCEN-*C*2/*c* does not agree particularly well with any member of the quadrilateral but agrees most well with *C*2/*c*-clinoferrosilite. Over the observed

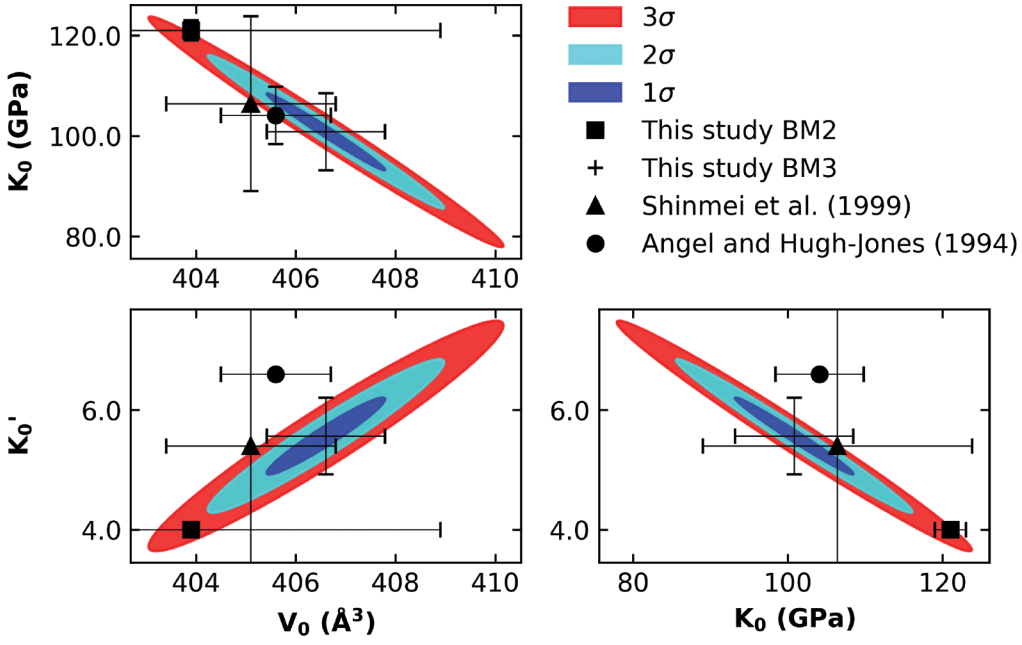

FIGURE 4. Confidence ellipses of isothermal equation of state parameters for third-order Birch-Murnaghan equation of state. The square symbol shows parameters obtained using the second-order equation. Both fits in this study combine the current data set with the lower-pressure data of Angel and Hugh-Jones (1994). Error bars correspond to one sigma. (Color online.)

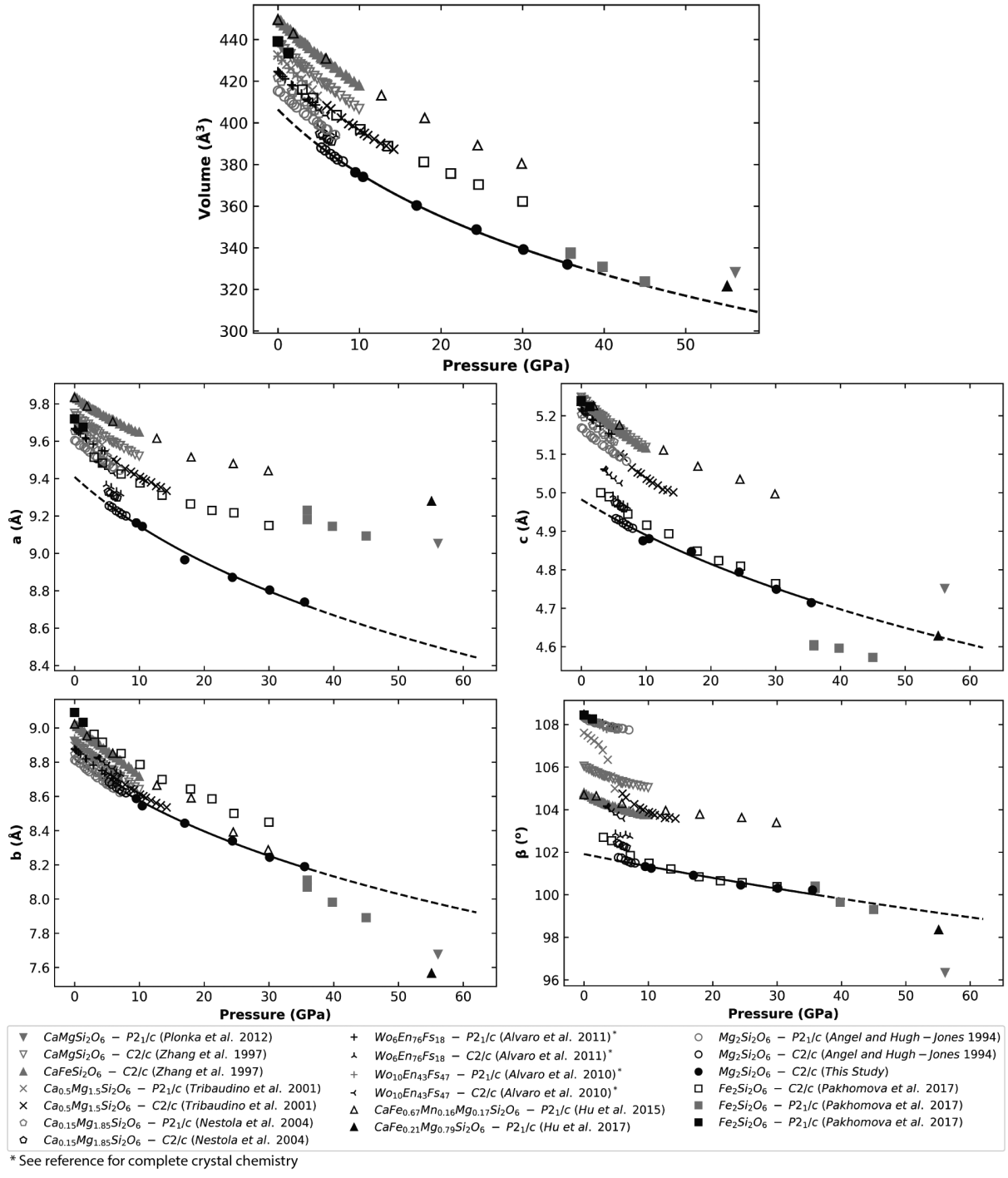

Figure 5. Compression data for phases within the hedenbergite-diopside-ferrosilite-enstatite quadrilateral. Solid line represents the Birch-Murnaghan EoS fits to the current experimental data for HPCEN, extrapolated beyond the data points with dashes.

pressure range evolution of *C*2/*c*-clinoferrosilite lattice parameters *c* and β agree remarkably well with those of HPCEN-*C*2/*c*.

HPCEN-*C*2/*c* high-pressure structure behavior

Structure refinements obtained at six pressure points between 9.5 and 35.5 GPa show the crystal maintained a *C*2/*c* space group symmetry throughout the pressure range. The structure of the HPCEN-*C*2/*c* phase is composed of three distinct polyhedra: one $Si1O_4$ tetrahedron and two octahedra, $Mg1O_6$ and $Mg2O_6$. The Si1 site is bonded to four oxygen atoms: O1, O2, O3A, and O3B. The bridging O3 atoms connect the chains of Si tetrahedra running parallel to the *c* crystallographic axis. The extremely kinked

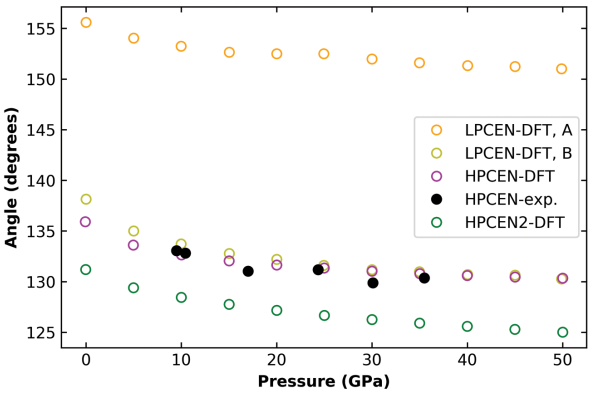

FIGURE 6. O3-O3-O3 angle (solid dots), a measure of rotation of Si tetrahedral units along the pyroxene chains. The kinking angle reduces by 2% over the experimental pressure range as the (001) axis shortens. (Color online.)

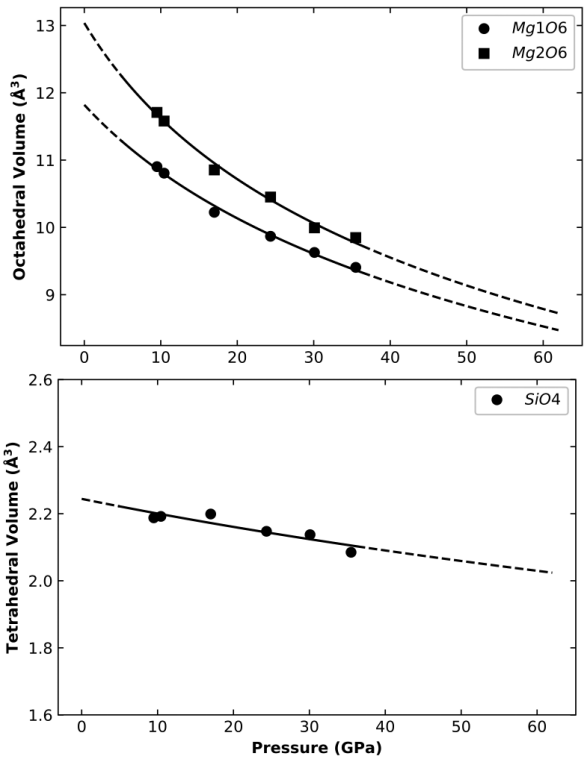

FIGURE 7. Pressure-volume trends of octahedral (Mg) and tetrahedral (Si) sites in HPCEN in *C*2/*c*. Solid lines represent the second-order Birch-Murnaghan EoS fits.

and O-rotated Si tetrahedral chain is a distinguishing feature of the HPCEN-*C*2/*c* phase. The O3-O3-O3 bond angle, a measure of rotation of individual Si tetrahedra, displays a decreasing trend with increasing pressure as seen in Figure 6. As the *c* axis shortens with increasing pressure, the Si tetrahedra rotate forcing the O3-O3-O3 angle to decrease, by 2% over the observed pressure range, as the chain becomes increasingly kinked. The Si tetrahedra are non-ideal, with Si1-O bond lengths ranging from 1.569(2) Å (Si1-O2) to 1.666(2) Å (Si1-O3B) at 9.5 GPa. Quadratic elongation and angular variation, measures of polyhedral ideality, are 1.0043 and 17.75°, respectively, at 9.5 GPa. The Mg1 atom, occupying the M1 site, sits at the center of the first of two MgO_6 octahedra. MgO_6 octahedra forms three unique bonds with O: Mg1-O1A, Mg1-O1B, and Mg1-O2. At 9.5 GPa, the Mg1-O1A, Mg1-01B, and Mg1-O2 bond lengths are 2.001(2), 2.07(2), and 1.989(2) Å, respectively. The M1 quadratic elongation and angular variation are 1.0059 and 19.18°. The M1 octahedra are edge-sharing along the O1B-O1B edge. Mg2 forms three unique bonds: Mg2-O1, Mg2-O2, and Mg2-O3. In the more distorted M2 octahedra the Mg2-O3 bond is the longest at 2.170(2) Å while Mg2-O1 is 2.068(2) Å and Mg2-O2 is 1.977(2) Å. The quadratic elongation and angular variation for the M2 site are 1.0097 and 25.82°.

The HPCEN-*C*2/*c* structure refinements show the SiO_4 tetrahedra remain relatively incompressible compared to the MgO_6 octahedra. Mg1 and Mg2 octahedra show a 13.8% and 15.9% volume reduction over the pressure range 9.5 to 35.5 GPa, respectively, while Si tetrahedra show only a 4.7% volume reduction. Octahedral and tetrahedral volumes as a function of pressure as well as polyhedral compressibility determined by a second-order Birch-Murnaghan equation of state are shown in Figure 7. The HPCEN-2 polyhedra follow the $\beta_{Mg2} = 14.3(1) \times 10^{-3} > \beta_{M1} = 10.3(7) \times 10^{-3} > \beta_{Si1} = 2.0(5) \times 10^{-3}$ GPa^{-1} scheme, where β represents the compressibility of the polyhedral units.

Within the relatively compressible Mg2 octahedron, the Mg1-O2 is the most compressible with $\beta_{Mg1\text{-}O2} = 11.7(7) \times 10^{-3}$, $\beta_{Mg1\text{-}O1A} = 5.9(8) \times 10^{-3}$ GPa^{-1}, and the edge-sharing Mg1-O1B is the stiffest bond $\beta_{Mg1\text{-}O1B} = 5.7(9) \times 10^{-3}$ GPa^{-1}. The deformed Mg2 bond compressibility values are: $\beta_{Mg2\text{-}O3} = 39.7(6) \times 10^{-3}$, $\beta_{Mg1\text{-}O2} = 11.7(8) \times 10^{-3}$, $\beta_{Mg1\text{-}O1} = 11(1) \times 10^{-3}$ GPa^{-1}. The high compressibility of the M2 octahedra, specifically the soft Mg2-O3 bond, accommodates much of the volume reduction over the observed pressure range. The compressed Mg octahedra, relative to the Si1 tetrahedra, allow for the rotation of Si tetrahedra from S-rotated to O-rotated chains during the LPCEN to HPCEN phase transition, occurring between 6.5 and 7.1 GPa (Angel et al. 1992; Jacobsen et al. 2010). As pressure increases, the Mg octahedra continue to compress, further accommodating the overall volume reduction.

The Si1 tetrahedra are far less compressible than the M octahedra, with a bulk modulus five times that of the M1 octahedra. The softest bond in the Si1 tetrahedra has a compressibility $\beta_{Si1\text{-}O1} = 3.4(4) \times 10^{-3}$ GPa^{-1} and the least compressible bond is the Si1-O2 bond with a compressibility of $\beta_{Si1\text{-}O1} = 0.6(2) \times 10^{-3}$ GPa^{-1}. Given the stiffness of the Si1 tetrahedra, the majority of the deformation in the tetrahedral chain is absorbed by the shrinking O3-O3-O3 bond angle. In addition to the non-polyhedral volume, overall compression of the HPCEN-*C*2/*c* unit cell with pressure can then be summarized as being governed by the compression of Mg octahedra, primarily on the M2 site, and rotation of Si1 tetrahedra decreasing the O3-O3-O3 bond angle.

Unlike in the orthopyroxene system, we do not find a significant increase in stiffness with increasing Ca^{2+} substitution into the M2 octahedral site. Hugh-Jones and Angel (1997) observed an increase in K_{T0} of 14% with the substitution of very small amounts of Ca^{2+} into the M2 site. However, in comparison with the results of Tribaudino et al. (2000) who examined the high-pressure behavior of Ca-rich HPCEN up to 35.5 GPa, we only notice a difference of 2.7% in K_{T0} between the two end-members.

This promotes the validity of the use of pure end-member $MgSiO_3$ as a representative pyroxene in the Earth's upper mantle, within the diopside-enstatite solid solution.

HPCEN-*C*2/*c* to HPCEN2-*P*2$_1$/*c* phase transition

Above 35.5 GPa, HPCEN undergoes a first-order phase transition to a HPCEN-*P*2$_1$/*c* phase. Data quality from our single pressure point is too low to report a structure refinement. However, in strong agreement with our observations, our DFT calculations predict a phase transition to a *P*2$_1$/*c* phase at 35 GPa (Fig. 8). Lattice parameters from our DFT calculations are compared to observations in Table 4.

Three phases were considered in the DFT calculations: LPCEN, HPCEN, and HPCEN2. Starting models for structure optimizations were taken from the crystallographic refinements performed in this study at 0 GPa for LPCEN, 10.4 GPa for HPCEN, and for HPCEN2 we adopted the *P*2$_1$/*c* high-pressure clinoferrosilite model reported by (Pakhomova et al. 2017). Structures of all three phases were fully optimized (all unit-cell parameters and fractional atomic coordinates) at a set of fixed external pressures from 0 to 50 GPa, with 5 GPa intervals. The GGA approximation is known to overestimate both the unit-cell parameters, as well as the phase transition pressures; however, as reported in Table 4, we obtained a reasonably good agreement with experimental results.

Our calculations predict that at 0 K the HPCEN structure becomes energetically favorable over the LPCEN structure at about 5 GPa, which is consistent with experimental observations. The transformation from HPCEN to HPCEN2 is predicted at approximately 35 GPa, which is slightly lower than the experimental observation (45 GPa), but reasonable for the GGA approximation.

Implications

Observation of the HPCEN2 phase in $Mg_2Si_2O_6$ completes the third apex of the pyroxene quadrilateral wherein HPCEN2 is found, facilitating a broader view of clinopyroxene crystal chemistry at conditions relevant to metastability in the Earth's mantle along cold subduction geotherms. In addition, the wide pressure stability of the *C*2/*c* phase may become significant when considering slab mineralogy and morphology. Similarly, the *C*2/*c* diopside end-member displays a continuous compression trend up to 45.6 GPa (Zhang et al. 1997; Tribaudino et al. 2000; Plonka et al. 2012) prior to transforming to the high-pressure *P*2$_1$/*c* structure. At 1650 °C, nearly all clinopyroxenes transform to garnet by 20 GPa (Gasparik 1989). However, it has been shown that the pyroxene-garnet transformation can be significantly inhibited at low temperature (<1550 °C) (Nishi et al. 2008). Pyroxenes subducted into the mantle by cold downwelling slabs could potentially be kept below temperatures of 1500 °C down to depths of ~1000 km (Bina et al. 2001).

As all of our experiments were performed at room temperature, the most that we can say about the thermal effects is that previous work (Nishi et al. 2008; Van Mierlo et al. 2013) has indicated that pyroxenes may persist metastably to ~1500 °C, temperatures corresponding to depths well into the ambient mantle transition zone and even deeper for cold slabs. To this, we can now add knowledge of the structure and elastic properties of metastable clinoenstatite (at 300 K) to at least 35 GPa, pressures well into the top of the lower mantle. The structures and elastic properties of metastable pyroxenes are necessary for the modeling of slab dynamics driven by density and therefore buoyancy forces. However, the temperature effects on metastable phases must first be determined. Therefore, further studies are required to constrain the transformation temperatures of HPCEN to HPCEN2 at high pressure as well as the implications of pyroxene metastability on slab dynamics in the mantle.

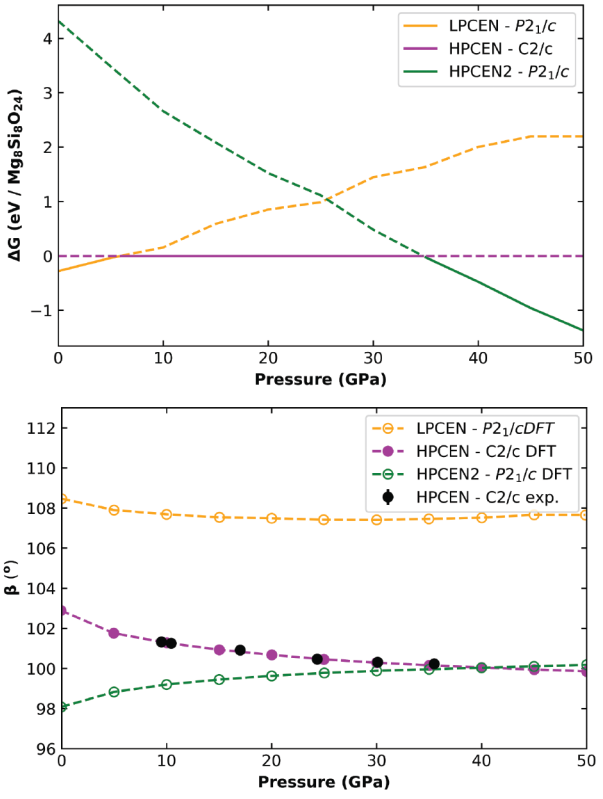

Figure 8. Density functional theory (DFT) results for the $Mg_8Si_8O_{24}$ system. (**top**) Change in Gibbs free energy was calculated to determine phase transition pressures for clinoenstatite showing a calculated phase transition from HPCEN to HPCEN2 at approximately 35 GPa. (**bottom**) Experimental measurements agree well with calculated structure parameters. (Color online.)

Table 4. Coefficients obtained from fitting a Birch-Murnaghan EoS

	LPCEN-DFT *P*2$_1$/*c*	HPCEN *C*2/*c*	HPCEN-DFT *C*2/*c*	HPCEN2 *P*2$_1$/*c*	HPCEN2-DFT *P*2$_1$/*c*
a_0 (Å)	9.7271	9.4389	9.5082	–	9.4665
a_{50}	9.0531	8.5831	8.7533	8.688(2)	8.7605
b_0 (Å)	8.9233	8.8450	8.9345	–	8.4573
b_{50}	8.0766	8.0519	8.1040	7.828(1)	7.9189
c_0 (Å)	5.2224	4.9739	5.0535	–	4.9209
c_{50}	4.8182	4.6336	4.6982	4.5840(9)	4.6096
β_0 (°)	108.46	101.91	102.89	–	98.08
β_{50}	107.65	99.36	99.86	100.46(2)	100.18
V_0 (Å^3)	429.96	406(1)	418.47	–	390.06
V_{50}	335.71	316.92	328.36	306.6(1)	314.74
K_{T0} (GPa)	107(1)	103(8)	106(2)	–	138(1)
K_0' (GPa)	5.1(1)	5.3(7)	5.6(2)	–	4.89(9)
ρ_0 (g/cm^3)	3.102	3.28(1)	3.187	–	3.419
ρ_{50}	3.972	4.208	4.063	4.350	4.237

Notes: Parameters from extrapolation of equation of state; subscript 50 determined at 50 GPa.

Funding

This research was supported through grants from U.S. National Science Foundation EAR-1452344 and EAR-1853521 to S.D.J. and EAR-1722969 to P.D. Support was also provided by the Capital/DOE Alliance Center (CDAC). Development of the ATREX software used for data analysis was supported by NSF grant EAR1440005. Portions of this work were performed at HPCAT (Sector 16) of the Advanced Photon Source (APS), Argonne National Laboratory. HPCAT operations are supported by DOE-NNSA under Award No. DE-NA0001974, with partial instrumentation funding by NSF. The Advanced Photon Source is a U.S. Department of Energy (DOE) Office of Science User Facility operated for the DOE Office of Science by Argonne National Laboratory under Contract No. DE-AC02-06CH11357. We thank Joshua Townsend for discussions and Sergey Tkachev for gas-loading diamond-anvil cells in the GSECARS gas-loading system, which is supported by COMPRES, the Consortium for Materials Properties Research in Earth Sciences under NSF Cooperative Agreement EAR 1606856.

References cited

Agrusta, R., Van Hunen, J., and Goes, S. (2014) The effect of metastable pyroxene on the slab dynamics. Geophysical Research Letters, 41(24), 8800–8808. http://doi.org/10.1002/2014GL062159

Akaogi, M., and Akimoto, S. (1977) Pyroxene-garnet solid-solution equilibria in the systems $Mg_3Si_4O_{12}$-$Mg_3Al_2Si_3O_{12}$ and $Fe_4Si_4O_{12}$-$Fe_3Al_2Si_3O_{12}$ at high pressures and temperatures. Physics of the Earth and Planetary Interiors, 15, 90–106.

Akashi, A., Nishihara, Y., Takahashi, E., Nakajima, Y., Tange, Y., and Funakoshi, K. (2009) Orthoenstatite/clinoenstatite phase transformation in $MgSiO_3$ at high-pressure and high-temperature determined by in situ X-ray diffraction: Implications for nature of the X discontinuity. Journal of Geophysical Research, 114, B04206.

Angel, R.J., and Hugh-Jones, D.A. (1994) Equations of state and thermodynamic properties of enstatite pyroxenes. Journal of Geophysical Research, 99(B10), 19777–19783.

Angel, R.J., Chopelas, A., and Ross, N.L. (1992) Stability of high-density clinoenstatite at upper-mantle pressures. Nature, 355, 322–324.

Angel, R.J., Gonzalez-Platas, J., and Alvaro, M. (2014) EosFit7c and a Fortran module (library) for equation of state calculations. Zeitschrift für Kristallographie, 229(5), 405–419.

Bevington, P.R., and Robinson, D.K. (2003) Data Reduction and Error Analysis for the Physical Sciences, 3rd ed. McGraw-Hill.

Bina, C.R. (2013) Mineralogy: Garnet goes hungry. Nature Geoscience, 6(5), 335–336.

Bina, C.R., Stein, S., Marton, F.C., and Van Ark, E.M. (2001) Implications of slab mineralogy for subduction dynamics. Physics of the Earth and Planetary Interiors, 127(1–4), 51–66.

Blöchl, P.E. (1994). Projector augmented-wave method. Physical Review B, 50(24), 17953–17979. https://doi.org/10.1103/PhysRevB.50.17953

Cottaar, S., Heister, T., Rose, I., and Unterborn, C. (2014) BurnMan: A lower mantle mineral physics toolkit. Geochemistry, Geophysics, Geosystems, 15(4), 1164–1179.

Dera, P., Zhuravlev, K., Prakapenka, V., Rivers, M.L., Finkelstein, G.J., Grubor-Urosevic, O.,Tschaunder, O., Clark, S.M., and Downs, R.T. (2013) High pressure single-crystal micro X-ray diffraction analysis with GSE_ADA/RSV software. High Pressure Research, 33(3), 466–484.

Deuss, A., and Woodhouse, J.H. (2004) The nature of the Lehmann discontinuity from its seismological Clapeyron slopes. Earth and Planetary Science Letters, 225, 295–304. https://doi.org/10.1016/j.epsl.2004.06.021

Ferot, A., and Bolfan-Casanova, N. (2012) Water storage capacity in olivine and pyroxene to 14 GPa: Implications for the water content of the Earth's upper mantle and nature of seismic discontinuities. Earth and Planetary Science Letters, 350, 218–230. https://doi.org/10.1016/j.epsl.2012.06.022

Finkelstein, G.J., Dera, P.K., and Duffy, T.S. (2015) Phase transitions in orthopyroxene (En_{90}) to 49 GPa from single-crystal X-ray diffraction. Physics of the Earth and Planetary Interiors, 244, 78–86.

Gasparik, T. (1989) Transformation of enstatite-diopside-jadeite pyroxenes to garnet. Contributions to Mineralogy and Petrology, 102, 389–405.

Hogrefe, A., Rubie, D.C., Sharp, T.G., and Seifert, F. (1994) Metastability of enstatite in deep subducting lithosphere. Nature. https://doi.org/10.1038/372351a0.

Hu, Y., Dera, P., and Zhuravlev, K. (2015) Single-crystal diffraction and Raman spectroscopy of hedenbergite up to 33 GPa. Physics and Chemistry of Minerals, 42(7), 595–608.

Hu, Y., Kiefer, B., Bina, C.R., Zhang, D., and Dera, P.K. (2017) High-pressure γ-$CaMgSi_2O_6$: Does penta-coordinated silicon exist in the Earth's mantle? Geophysical Research Letters, 44, 11,340–11,348.

Hugh-Jones, D.A., and Angel, R.J. (1997) Effect of Ca^{2+} and Fe^{2+} on the equation of state of $MgSiO_3$ orthopyroxene. Journal of Geophysical Research, 102, 12,333–12,340.

Jacobsen, S.D., Liu, Z., Boffa Ballaran, T., Littlefield, E.F., Ehm, L., and Hemley, R.J. (2010) Effect of H_2O on upper mantle phase transitions in $MgSiO_3$: Is the depth of the seismic X-discontinuity an indicator of mantle water content? Physics of the Earth and Planetary Interiors, 183(1–2), 234–244.

King, S.D., Frost, D.J., and Rubie, D.C. (2015) Why cold slabs stagnate in the transition zone. Geology, 43(3), 231–234. https://doi.org/10.1130/G36320.1

Kresse, G., and Hafner, J. (1993) Ab initio molecular dynamics for open-shell transition metals. Physical Review B, 48(17), 48–51.

Kung, J., Li, B., Uchida, T., Wang, Y., Neuville, D., and Liebermann, R.C. (2004) In situ measurements of sound velocities and densities across the orthopyroxene high-pressure clinopyroxene transition in $MgSiO_3$ at high pressure. Physics of the Earth and Planetary Interiors, 147(1), 27–44.

Mao, H.K., Xu, J., and Bell, P.M. (1986) Calibration of the ruby pressure gauge to 800 kbar under quasi-hydrostatic conditions. Journal of Geophysical Research, 91(B5), 4673–4676.

Morimoto, N., Fabries, J., Ferguson, A.K., Ginzburg, I.V., Ross, M., Seifeit, F.A., and Zussman, J. (1989) Nomenclature of pyroxenes. Canadian Mineralogist, 2(5), 198–221.

Nestola, F., Tribaudino, M., and Boffa Ballaran, T. (2004) High pressure behavior, transformation and crystal structure of synthetic iron-free pigeonite. American Mineralogist, 89, 189–196.

Nishi, M., Kato, T., Kubo, T., and Kikegawa, T. (2008) Survival of pyropic garnet in subducting plates. Physics of the Earth and Planetary Interiors, 170(3–4), 274–280.

Nishi, M., Kubo, T., Ohfuji, H., Kato, T., Nishihara, Y., and Irifune, T. (2013) Slow Si-Al interdiffusion in garnet and stagnation of subducting slabs. Earth and Planetary Science Letters, 361, 44–49. https://doi.org/10.1016/j.epsl.2012.11.022

Pacalo, R.E.G., and Gasparik, T. (1990) Reversals of the orthoenstatite-clinoenstatite transition at high pressures and high temperatures. Journal of Geophysical Research, 95(90).

Pakhomova, A., Ismailova, L., Bykova, E., Bykov, M., Boffa Ballaran, T., and Dubrovinsky, L. (2017) A new high-pressure phase transition in clinoferrosilite: In situ single-crystal X-ray diffraction study. American Mineralogist, 102, 666–673.

Perdew, J.P., Burke, K., and Ernzerhof, M. (1996) Generalized gradient approximation made simple. Physical Review Letters, 77(18), 3865–3868. https://doi.org/10.1103/PhysRevLett.77.3865

Plonka, A.M., Dera, P., Irmen, P., Rivers, M.L., Ehm, L., and Parise, J.B. (2012) β-diopside, a new ultrahigh-pressure polymorph of $CaMgSi_2O_6$ with six-coordinated silicon. Geophysical Research Letters, 39, 2000–2003.

Poldervaart, A., and Hess, H.H. (1951) Pyroxenes in the crystallization of basaltic magma. The Journal of Geology, 59(5), 472–489.

Revenaugh, J., and Jordan, T.H. (1991) Mantle layering from ScS reverberations 3. The upper mantle. Journal of Geophysical Research, 96, 19781–19810.

Ringwood, A.E. (1976) Phase transformations in descending plates and implications for mantle dynamics. Tectonophysics, 32(1–2), 129–143. https://doi.org/10.1016/0040-1951(76)90089-5

Rivers, M.L., Prakapenka, V.B., Kubo, A., Pullins, C., Hall, C.M., and Jacobsen (2008) The COMPRES/GSECARS gas loading system for diamond anvil cells at the Advanced Photon Source. High Pressure Research, 28(3), 273–292.

Ross, N.L., and Reynard, B. (1999) The effect of iron on the $P2_1/c$ to $C2/c$ transition in $(Mg,Fe)SiO_3$ clinopyroxenes. European Journal of Mineralogy, 11(3), 585–589.

Sheldrick, G.M. (2008) A short history of SHELX. Acta Crystallographica, A64, 112–122.

Shinmei, T., Tomioka, N., Fujino, K., Kuroda, K., and Irifune, T. (1999) In situ X-ray diffraction study of enstatite up to 12 GPa and 1473 K and equations of state. American Mineralogist, 84, 1588–1594.

Shiraki, K., Kuroda, N., Urano, H., and Maruyama, S. (1980) Clinoenstatite in boninites from the Bonin Islands, Japan. Nature, 285, 31–32.

Tribaudino, M., Prencipe, M., Bruno, M., and Levy, D. (2000) High-pressure behaviour of Ca-rich $C2/c$ clinopyroxenes along the join diopside-enstatite ($CaMgSi_2O_6$-$Mg_2Si_2O_6$). Physics and Chemistry of Minerals, 27(9), 656–664.

Tribaudino, M., Prencipe, M., Nestola, F., and Hanfland, M. (2001) A $P2_1/c$-$C2/c$ high-pressure phase transition in $Ca_{0.5}Mg_{1.5}Si_2O_6$ clinopyroxene. American Mineralogist, 86, 807–813.

Ulmer, P., and Stalder, R. (2001) The $Mg(Fe)SiO_3$ orthoenstatite-clinoenstatite transitions at high pressures and temperatures determined by Raman-spectroscopy on quenched samples. American Mineralogist, 86, 1267–1274.

Van Mierlo, W.L., Langenhorst, F., Frost, D.J., and Rubie, D.C. (2013) Stagnation of subducting slabs in the transition zone due to slow diffusion in majoritic garnet. Nature Geoscience, 6(5), 400–403. https://doi.org/10.1038/ngeo1772

Yu, Y.G., and Wentzcovitch, R.M. (2009) Low-pressure clino- to high-pressure clinoenstatite phase transition: A phonon-related mechanism. American Mineralogist, 94, 461–466. https://doi.org/10.2138/am.2009.3071

Zhang, L., Ahsbahs, H., Hafner, S.S., and Kutoglu, A. (1997) Single-crystal compression and crystal structure of clinopyroxene up to 10 GPa. American Mineralogist, 82, 245–258.

Manuscript received July 19, 2018
Manuscript accepted January 30, 2019
Manuscript handled by Oliver Tschauner

Endnote:

[1]Deposit item AM-19-66740, CIF. Deposit items are free to all readers and found on the MSA website, via the specific issue's Table of Contents (go to http://www.minsocam.org/MSA/AmMin/TOC/2019/Jun2019_data/Jun2019_data.html).